



Hierarchical Cu-Rich Nanoprecipitates in a CoFeTiVCu High-Entropy Alloy and Its Impressed Strength-Plasticity Balance

Lu Wang^{1,2} · Chenxi Gu¹ · Cun Zhang¹ · Zhengzhong Feng¹ · Jiaojiao Yi¹

Received: 31 August 2022 / Accepted: 9 November 2022 / Published online: 10 December 2022
© The Author(s) under exclusive licence to The Korean Institute of Metals and Materials 2022

Abstract

Structural diversity, like chemical composition and morphology, is an important originating point of various mechanical properties. The exploration of these properties has been motivated by the fertile compositional constituents of multicomponent alloys/high-entropy alloys (HEAs). Herein, hierarchical Cu-rich precipitates embedded in a BCC matrix were found and highlighted in an equimolar CoFeTiVCu HEA. The Cu-rich precipitates were branched into two main classifications: nanoscale particles and micron lath/irregular shapes. Among them, the nanoparticles were almost evenly distributed in the overall region, which was attributed to the dramatically decreased solubility of Cu in the BCC matrix as the temperature decreased and that Cu quickly diffused. Alternatively, the others formed directly from the Cu-rich liquid during the solidification process. These kinds of hierarchical precipitates, combined with the great solid solution strengthening in the BCC matrix, gave rise to an excellent combination of strength and plasticity, specifically a yield strength, fracture strength, and compressive plasticity as high as 1.9 GPa, 2.2 GPa, and 7%, respectively.

Keywords High-entropy alloy · Precipitation strengthening · Microstructure · Mechanical properties

1 Introduction

As an important milestone in the field of metallurgy, HEAs have attracted considerable attention in the past decades, dramatically broadening the realm of alloy compositions [1–3]. This kind of blooming composition diversity has directly resulted in significant breakthroughs, providing a potential route to overcome the challenges of traditional metallurgical dilemmas. For example, some HEAs with five or even more principal elements, such as AlCoCrFeNi and HfMoTaTiZrNb_x ($x = 0, 1$), unexpectedly possess a single-phase structure under the influence of high mixing entropy. Moreover, some of them exhibit excellent synergy in strength and plasticity [4, 5]. However, the relatively monotonous strengthening mechanism, i.e., solid solution strengthening, in single-phase HEAs causes a non-negligible

bottleneck in improved strength. The yield strength of high plastic single-phase FCC CoCrCuFeNiTi_x ($x = 0–0.5$) HEAs is improved with increasing Ti content, but it is still less than 700 MPa [6]. Naturally, inducing a secondary phase in single-phase HEAs has drawn much attention and successfully enhanced the strength without sacrificing ductility by strictly controlling the physical details of the secondary phase (shape, amount, distribution etc.) [7–11].

Among all factors associated with the numerous secondary phases, nanoscale features commonly show an attractive advantage in acquiring the comprehensive mechanical properties of HEAs [12]. Nano-sized Al–Ni rich B2 phases with different sizes (~ 18 and 70 nm) formed in the FCC dendritic matrix and the BCC inter-dendrites of the Al_{0.5}CoCrFeNi alloy undergoing a simple heat treatment of aging at 650 °C for 8 h greatly increase the yield strength and ultimate tensile strength to 834 and 1220 MPa, respectively, from 355 and 714 MPa of the alloy without nanoprecipitates [7]. Likewise, through multiple thermomechanical treatments, the superb mechanical behavior of multi-phase (FeCoNi)₈₆–Al₇Ti₇ alloy has been achieved by introducing 50%–55% volume fraction ductile (Ni, Co, Fe)₃(Ti, Al) L1₂ nanoparticles (~ 50 nm) in the FCC matrix. Specifically, its strength and elongation are dramatically improved by 750% and 166% to as high

✉ Jiaojiao Yi
yijiaojiao2006@163.com

¹ Laboratory of Advanced Multicomponent Materials, School of Mechanical Engineering, Jiangsu University of Technology, Changzhou 213001, China

² School of Materials Engineering, Jiangsu University of Technology, Changzhou 213001, China

as 1.5 GPa and 50% compared to the FeCoNi-base alloy [12]. The common feature of these nanoprecipitates is that all they originate from multicomponent intermetallic compounds. However, an alternative nanoprecipitate only with one main principal element has also shown enormous potential in optimizing the mechanical properties of HEAs. For instance, 50-nm Cu-rich nanoparticles precipitate from the (Cu, Mn)-rich FCC supersaturated solid solution in the CrMnFeCoNiCu HEAs, which doubles the alloy's yield strength to 350 MPa without sacrificing its plasticity [13].

In essence, the formation of Cu-rich precipitates in HEAs closely links with the coupling between the positive mixing enthalpies of Cu and other elements and the low melting temperature of Cu. From the thermodynamic stability, the positive mixing enthalpies of Cu with other constituents cause high Gibbs free energies of the mixing system and lead to the formation of Cu-lean phase and Cu-rich phases [14]. If the constituent elements had different melting points, the elements with a high melting point preferentially solidify to form dendrites or a matrix while those with a low melting point might form inter-dendrites or precipitates in the matrix during solidification [15]. Those immediately result in the Cu being expelled from the primary phase and eventually solidifying in the inter-dendrites and form precipitated phases [16, 17]. Nevertheless, the existing form of Cu is not fixed and exactly able to be tailored by composition design and manufactured process [13, 18, 19]. Actually, spherical, rod-like, and plate-like Cu-rich nanoprecipitates have been widely detected in the reported HEAs, such as multi-phase AlCoCuFeNi and AlCoCrCuFeNi HEAs [15, 18]. Particulate and irregular Cu-rich phases have been formed in Fe–Mn–Cr–Co-base HEAs with varying concentrations of Cu [20, 21]. Therefore, by modulating alloy compositions, more fertile morphologies of Cu-rich precipitates might be developed. In the present work, an interesting hierarchical structure associated with Cu-rich precipitates was found in a CoFeTiVCu HEA. With the consideration of hierarchical structure benefiting the mechanical properties, the microstructural morphology and its impact on the mechanical properties of the CoFeTiVCu HEA have been highlighted and intensively investigated. Results show that the hierarchical Cu-rich precipitates in a homogeneous BCC matrix might be an important origination of an excellent strength-plasticity synergy of the currently studied alloy.

2 Experimental Procedures

Alloy ingots were fabricated on a water-cooled copper crucible using arc melting under a titanium getter argon atmosphere. The purities of all raw materials were greater than 99.9 wt%. Remelting was conducted at least four times to ensure the chemical homogeneity of alloy ingots. Ingots

were melted and poured into a rod-shaped copper mold with a diameter of 4 mm and height of 60 mm. The actual chemical composition of the rod-like samples was determined as $\text{Co}_{19.9}\text{Fe}_{20.0}\text{Ti}_{21.0}\text{V}_{20.3}\text{Cu}_{18.8}$ based on energy dispersive X-ray spectrometry (EDS, Oxford instrument), which is consistent with its nominal composition.

The crystal structures of the samples were identified by a PANalytical X'Pert X-ray diffractometer (XRD) with Cu $K\alpha$ radiation from 20° to 100° at a scanning rate of $1^\circ/\text{min}$. The microstructural morphologies were characterized on the cross-section of the rod-like specimens by field emission scanning electron microscopy (FESEM, Zeiss Sigma 500) equipped with EDS. The secondary electron SEM morphological images were captured under an electron high tension (EHT) voltage of 20 kV and a working distance of ~ 8.5 mm. Electron backscattered scattering diffraction (EBSD, Oxford) analysis of the samples was performed using an HKL-Technology EBSD system. Thermal parameters, such as the phase transition and liquidus temperature, were determined by differential scanning calorimetry (DSC, Netzsch 404 F3) under Ar atmosphere. The heating and cooling rates were set as 30 K/min.

Uniaxial compressive tests were conducted by a universal testing machine (UTM5305-G, Suns) at RT with a constant strain rate of $1 \times 10^{-3} \text{ s}^{-1}$. The dimensions of the tested specimens were 3.7 mm in diameter and ~ 5.7 mm in height. Vickers hardness measurements were carried out by a Vickers microhardness tester (HVS-1000B, Sanfeng) with a load of 200 g and a dwell time of 15 s. The average value was obtained on the polished cross-section surfaces of each specimen through at least ten measurements.

3 Results and Discussion

For most 3d transition metal (TM) HEAs, the elemental Cu is generally reduced to a special existence and is based on linking Cu-containing precipitates since the mixing enthalpies of Cu with other 3d TM elements are commonly positive [22] (see Table 1) and the melting point of Cu is relatively low. Moreover, the morphologies of Cu precipitates are not invariable. For instance, rhombohedron-shaped Cu precipitates with a content of Cu up to 58.8 ± 3 at% are widely observed in AlCoCrCuFeNi, while Cu precipitates are nano-spherical and rod-like shape with 50–75 at% Cu

Table 1 Mixing enthalpies of element pairs ΔH_{mix} (kJ/mol) in the CoFeTiVCu HEA [22]

ΔH_{mix}	Fe	Ti	V	Cu
Co	– 1	– 28	– 14	6
Fe	–	– 17	– 7	13
Ti	–	–	– 2	– 9
V	–	–	–	5

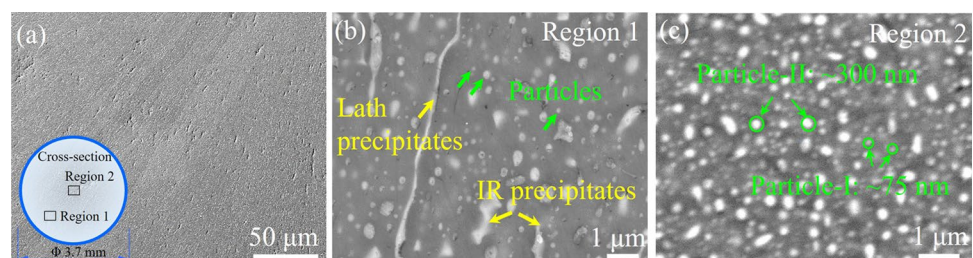
in FeCoNiCuAl HEAs [18, 23]. Thus, in considering the important dependence of mechanical properties on microstructural morphology, exploring new Cu-incorporated microstructures and determining its origination seem to be significant in understanding the role of Cu in HEAs. Accordingly, in the present work, the microstructure of a novel Cu-containing HEA CoFeTiVCu was intensively investigated and showed that the morphology of the Cu precipitates displayed a special hierarchical feature, as shown in Fig. 1. Overall, two distinct regions, i.e., the gray matrix and bright precipitates, can be easily seen in the columnar crystal structure of the CoFeTiVCu HEA (Fig. 1a). In previous literature, bright precipitates are likely to be Cu-incorporated phase. For more details, the magnified images of local regions in the sample's cross-section (inset of Fig. 1a) show that even for bright precipitates different morphologies are still distinguishable. As shown in Fig. 1b, c, we can bifurcate the bright precipitates into two main classifications according to their shapes: small particles with a wide size range of 10^1 – 10^2 nm (green arrows in Fig. 1b) that uniformly precipitate in the whole matrix; lath and irregular (IR) precipitates (yellow arrows) with thicknesses less than 1 μm generally growing along the radial direction from the cylindrical surface to the center. Interestingly, lath and irregular precipitates were mainly distributed to the outside of the specimens, but in the center, only fine particles, i.e., nanoprecipitates, with a size range of 50–400 nm were evenly distributed in this area (Fig. 1c). Additionally, columnar crystals formed in the outer regions during solidification process, while uniformly fine particles existed in the two regions indicating that they might precipitate from the matrix due to the decreasing solid solution as the temperature decreases during solidification. Furthermore, even only for the bright precipitates, two-hierarchical nanoprecipitates were present in the overall SEM images (Fig. 1c), and their average sizes were about 75 nm and 300 nm, respectively (particle-I and particle-II).

To determine the composition of the different regions, such as matrix and precipitates, in the currently studied CoFeTiVCu HEA, EDS mapping and point scanning were employed simultaneously as shown in Fig. 2. The overall elemental distribution proves that the bright regions, including lath, irregular precipitates, and nanoparticles, are composed of a Cu-rich phase, which agrees with previous

reports and our hypothesis, and the matrix is enriched with the other four elements. The representative EDS mapping of the central region of the specimens is shown in Fig. 2b–f. The specific data of their composition is depicted in Fig. 2g. Note that the average concentration of Cu was as high as 57.8 ± 4.4 at% in Cu-rich precipitates, which indicates that the formation of these precipitates is associated with a tendency to reject Cu from the matrix via decomposition with decreasing temperature during solidification [19, 24]. The other four constituent elements are homogeneously distributed in the matrix with an average concentration of ~ 22 at%. According to previous research [13, 25], uniformly dispersed nano-size Cu-rich precipitates in the matrix confirm the ability to effectively impede dislocation motion and enhance the strength in HEAs. Additionally, the hierarchical Cu-rich precipitates in the currently studied alloy should further strengthen the alloy. Therefore, it is reasonable to expect the currently studied alloy to possess relatively superior mechanical properties.

Figure 3a shows the representative engineering stress–strain curve of the CoFeTiVCu HEA. The critical mechanical properties, including yield strength ($\sigma_{0.2}$), fracture strength (σ_b), plastic strain (ϵ_p), and Vickers hardness (HV), are tabulated in Table 2. For comparison, some reported Co–Fe–Cu-based HEAs and BCC-structured HEAs with excellent properties [10, 23, 26–36] were also organized and summarized in Table 2. Accordingly, the yield strength versus plastic strain of all the mentioned alloys are plotted in Fig. 3b. Overall, the currently studied alloy possessed an attractive yield strength, exceeding some reported Co–Fe–Cu-based HEAs and BCC-structured HEAs. It suggests that the Cu-rich nanoparticles have a more prominent contribution to enhancing the yield strength compared with the Cu-rich precipitates with other morphologies or interdendrites formed in the mentioned Cu–Fe–Cu-based HEAs. Meanwhile, it has a relatively potential plasticity of around 7%. To comprehensively profile its mechanical behavior, the SEM fracture surface morphologies of the studied alloy provided some important clues, as shown in Fig. 3c, d. Note that the fracture behavior of the studied alloy is a typical cleavage fracture. As is well known, the failure behavior of an alloy originates from the excessive propagation of differently layered defects. During the deformation process,

Fig. 1 SEM bright-field images of the CoFeTiVCu alloy. **a** Relatively macro-microstructure of the sample cross-section with 1000 magnifications, **b–c** microstructures of the regions as marked in the inset of **a**



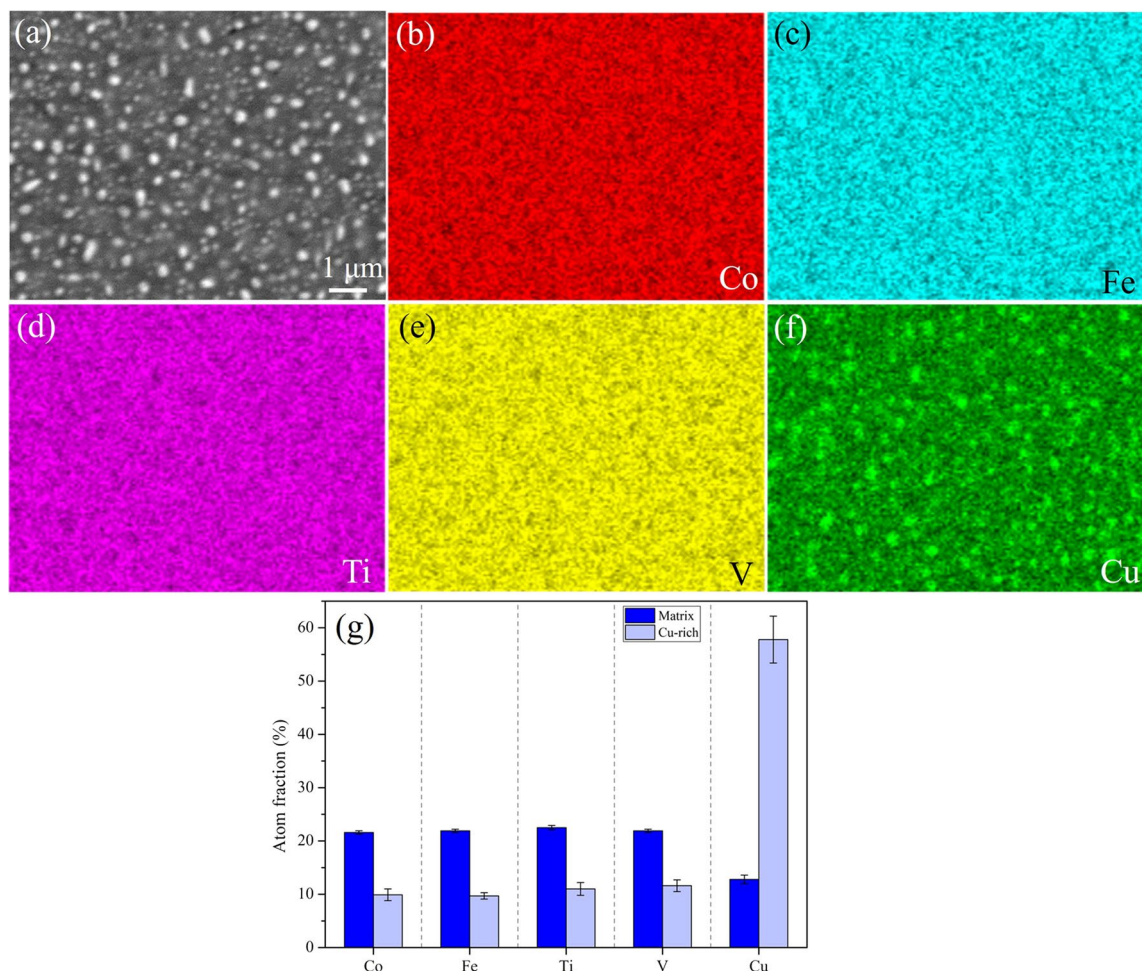


Fig. 2 SEM image of the CoFeTiVCu alloy **a**, EDS mapping of element Co, Fe, Ti, V, and Cu **b–f**, and the compositional analysis of the matrix and the Cu-rich phase **g**

the river pattern expanded outward in a fan-shaped manner from the crack source and formed dissociated fans. In the magnified image (Fig. 3d), many cleavage steps distinctly passed through vast bright Cu-rich regions, which confirms that the dispersed Cu-rich precipitates (especially for particle-II) contributed to the good plasticity due to the impediment of the crack extension. Likewise, the large plastic strain and high yield strength attributed to Cu-rich precipitates have been also observed in other HEAs, such as in FeCoNiCu and AlCoCrFeNiCu_{0.5} alloys [31, 37].

The strain hardening rate against true strain curve of the CoFeTiVCu HEA is shown in the inset of Fig. 3a, which exhibits a three-stage (stage I–III) work hardening characteristic. According to phase analysis, the alloy was mainly composed of BCC and FCC phases based on the XRD result. The exploration of the microstructural evolution has confirmed that dislocation slip controls the plastic deformation process before 10% strain in the FCC-structured HEAs [38, 39], and dislocation dominates the deformation at different strains if

the strain hardening rate curve exhibits a steady region in the BCC-structured HEAs [40–42]. Moreover, dislocation movement is more active in the soft FCC phase compared to the hard BCC/B2 phases in the multiphase HEAs [43, 44]. Thus, at the initial deformation stage (fast reduced-working rate region marked with stage I), the dislocations occur preferentially in the soft Cu-rich FCC phase; as the deformation amount increases (the steady region marked with stage II), the dislocations take place in both the FCC and BCC/B2 phases and the density of dislocation in the FCC is higher than that in the BCC/B2 phases. At the last deformation stage (stage III), the deformation inconsistency of FCC and BCC/B2 phase increases, resulting in the micro-cracks forming along two-phase interface, propagating, and then finally fracturing. The similar deformed mechanism and microstructural evolution have been observed in the BCC + FCC dual-phase multi-component alloys [45, 46].

Besides morphologies, the phase components and their contents are important aspects affecting mechanical

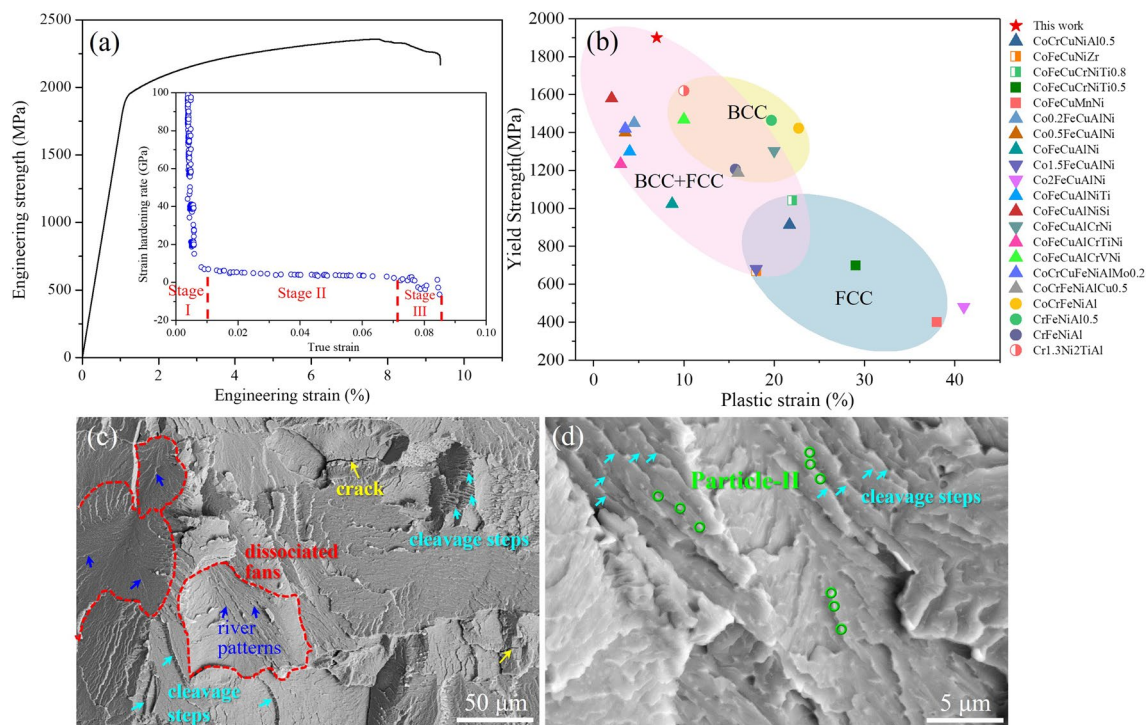


Fig. 3 Compressive engineering stress–strain curve of the CoFeTiVCu HEA **a** with the strain hardening rate ($d\sigma/d\varepsilon$) against true strain curve in the inset of **a**, yield strength versus plastic strain of

the studied alloy compared to some reported Co–Fe–Cu-based HEAs and BCC-structured HEAs **b**, and SEM fracture surface morphologies **c–d**

Table 2 The phase structure, yield strength ($\sigma_{0.2}$), fracture strength (σ_b), plastic strain (ε_p), and hardness (HV) of the CoFeTiVCu and some Co–Fe–Cu-based HEAs and BCC-structured HEAs [10, 23, 26–36]. IM represents for intermetallic phases

Alloys	Phase	$\sigma_{0.2}$ (MPa)	σ_b (MPa)	ε_p (%)	HV	Refs.
CoFeTiVCu	BCC + FCC	1900 ± 30	2300 ± 50	7 ± 0.5	512.6 ± 25.5	This work
CoFeCuAlNi	BCC + FCC	1023.6	1698.6	8.7	419.6 ± 19.5	[23]
CoFeCuAlNiTi	BCC + FCC	1300	1670	4	625	[23]
CoFeCuAlNiSi	BCC + FCC	1580	1930	2	680	[23]
CoFeCuAlCrNi	FCC + BCC	1303	2081	20	470	[23]
CoFeCuCrNiTi _{0.8}	FCC + IM	1042	1848	22	–	[26]
CoFeCuCrNiTi _{0.5}	FCC	700	1650	29	–	[27]
CoFeCuMnNi	FCC	400	950	38	–	[28]
Co _{0.2} FeCuAlNi	BCC + FCC	1450	1600	4.5	531.4	[29]
Co _{0.5} FeCuAlNi	BCC + FCC	1400	1550	3.5	544.9	[29]
Co _{1.5} FeCuAlNi	FCC + BCC	680	1100	18	366.4	[29]
Co ₂ FeCuAlNi	FCC + BCC	480	800	41	249.3	[29]
CoFeCuAlCrTiNi	BCC + FCC	1234	1356	3	–	[30]
CoFeCuAlCrVNi	BCC + FCC	1469	1970	10	–	[30]
CoCrFeNiAlCu _{0.5}	BCC + FCC	1187	1926	16	–	[31]
CoCrCuNiAl _{0.5}	BCC + FCC	913.8	1780	21.7	–	[32]
CoFeCuNiZr	FCC + IM	668	810	18	–	[33]
CoCrCuFeNiAlMo _{0.2}	BCC + FCC	1420	2240	3.5	–	[34]
Cr _{1.3} Ni ₂ TiAl	BCC + IM	1620	2600	10	–	[10]
CoCrFeNiAl	BCC	1423	2582	22.7	–	[35]
CrFeNiAl _{0.5}	BCC	1464	1608	19.7	228.94	[36]
CrFeNiAl	BCC	1205	1817	15.7	247.8	[36]

properties. Accordingly, XRD was performed to identify the actual phase components, as shown in Fig. 4a. The crystal peaks imply that the alloy CoFeTiVCu was primarily constituted of BCC and FCC phases. As expected, the diffraction peaks of the FCC matched well with Cu-type FCC phase according to the JCPDS card (PDF#04–0836). In other words, the bright precipitates possess a typical FCC structure. The indexes of crystal planes of each phase corresponding to the peaks are indicated in Fig. 4a. In addition to the BCC and FCC phases, a slight superlattice diffraction peak around 30° was observed, indicating that a small amount of BCC phase exhibited an ordered variant structure (B2). The ordered structure in this alloy theoretically corresponded to the CoTi B2 phase with the Pm-3m space group (PDF#65–6063) and lattice parameter of 0.298 nm [47]. In Cu–Co–Ti alloy system, there is a strongest tendency to form CoTi B2 phase among all the possible intermetallic compounds (CoTi, Co₂Ti, Co₃Ti, and CoTi₂) according to phase diagram and experimental results [48, 49]. For example, lots of (Co, Ti)-rich spherical particles with a diameter of 20 nm precipitate from the matrix in the Cu–Co–Ti alloy through rolled and aged treatments. These particles are composed of a CoTi B2 phase with the atomic ratio of Co and Ti close to 1, which has been confirmed by SAED and TEM-EDS analysis [47]. In addition, CoTi phase can directly form dendrites surrounding the Cr-rich phase in the CoCrCuTi HEA without any treatments [50]. The strong trend of forming CoTi B2 phase is attributed to the negative enthalpy of mixing between Co and Ti. Combined the precipitation behavior of CoTi B2 phase in the reported Cu–Co–Ti containing alloy system, it is quite natural that CoTi B2 phase easily solidifies from liquid in the studied CoFeTiVCu HEA from the viewpoint of thermodynamics. The lattice constants of the BCC, FCC, and B2 phases were determined as 0.297, 0.361, and 0.296 nm using the Rietveld refinement method, respectively. Different from the brittle nature of B2 intermetallic compound like NiAl, CoTi B2 phase exhibited a great amount of ductility [51], which should be one of the

origination of the superior ductility ($7 \pm 0.5\%$) of the CoFeTiVCu HEA.

Furthermore, to quantitatively determine the volume fraction of each phase and the crystalline character, EBSD was conducted on the cross-section of the cylindrical samples for the CoFeTiVCu HEA, as shown in Fig. 4b, c. The phase map (Fig. 4b) shows that two phases were detected in the microstructure, where the red and blue areas corresponded to the BCC and FCC phases. Their volume fractions were 82% and 18%, respectively. Figure 4c shows the inverse pole figure (IPF) map with the standard stereographic triangle in the bottom right-hand corner. It indicates that typical columnar crystals grew from the cylindrical surface to the center along with the preferred directions of $\langle 001 \rangle$ and $\langle 101 \rangle$ of the BCC phase. Generally, the formation of columnar crystals is attributed to the growth rate and preferred directions of crystals. For example, the microstructure of cylindrical rods for Al_{0.6}CoCrFeNi HEAs evolved from a columnar dendrite to an equiaxed grain with the cooling rate increasing from $\sim 10^2$ to 10^5 K s⁻¹ [52]; the microstructure of single BCC-structured CoFeNiTiV HEA exhibited a similar columnar crystal characteristic with $\langle 001 \rangle$ and $\langle 101 \rangle$ preferred directions [53]. According to the formula of cooling rate $V = 10/r^2$ and the radius of copper mold casting cylindrical sample r [54], the V of a 3.7 mm cylindrical sample was determined as $\sim 2.9 \times 10^2$ K s⁻¹, which provides a proper growth rate of BCC crystals with the preferred directions of $\langle 001 \rangle$ and $\langle 101 \rangle$ to form the columnar crystals in the relatively external regions of the cylindrical samples of the CoFeTiVCu HEA. Meanwhile, it is worth noting that part of the FCC phase grew along the grain boundaries and the other formed in the grain.

Actually, microscopic Cu segregation is difficult to be restrained even through water quenching, cold rolling, or annealing at high temperature, since Cu has highest positive mixing enthalpies with most elements in 3d TM HEAs. Thus, it is common that Cu-rich phases tend to form intragranular precipitates with diverse morphologies under

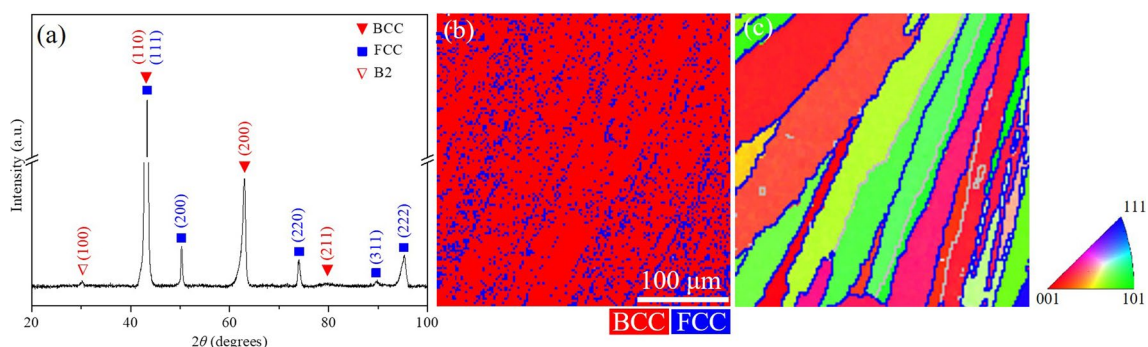


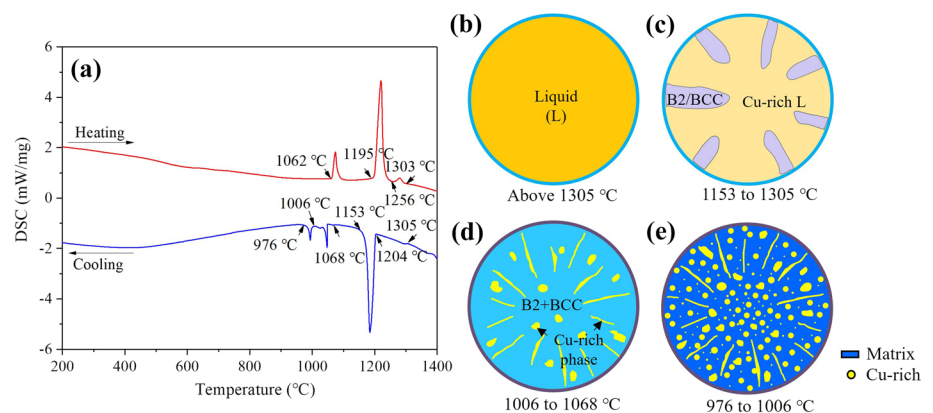
Fig. 4 XRD pattern **a**, phase map **b**, and inverse pole figure (IPF) map **c** with the corresponding standard stereographic triangle on the right hand of the CoFeTiVCu HEA

different processes in Cu-containing HEAs. For example, the plate-like Cu precipitates with the length of hundred nanometers are formed from matrix via a mechanism of spinodal decomposition in the Al–Co–Cr–Cu–Ni–(Fe) samples prepared by arc-melting and spark plasma sintering [18, 55]. When the samples are processed by plasma remelting with a high cooling rate, Cu-rich nanoparticles (~several nanometers) precipitate in the FCC dendritic matrix of the $\text{Al}_{0.5}\text{CoCrCuNi}$ HEA due to the sluggish diffusion of Cu [32]. These results indicate a rapid cooling rate can effectively regulate the morphology of Cu-rich phase, though it hardly suppresses the decomposition of metastable solid solution. In the currently studied CoFeTiVCu HEA prepared by a copper mold suction casting with a high cooling rate, Cu segregation occurs on different length scales: nanoscale particles (~75 nm particle-I and ~300 nm particle-II) and micron Cu-rich phase (lath and irregular shapes) (see Fig. 1). To profile the formation of various Cu-rich structures, high-temperature DSC tests from RT to 1400 °C were carried out and displayed in Fig. 5a. Three distinct endothermic events were noted in the heating process. The first peak around 1062 °C is consistent with the melting point of the Cu-rich FCC phase, which is in the same temperature range as those of the reported Cu-rich phase in the CoCrFeNiCu and $\text{Al}_x\text{CoCrFeNiCu}$ ($x=1-3$) HEAs [56, 57]. The high peak at 1195–1256 °C and the small peak at 1256–1303 °C are closely linked with the fusion of the major BCC and minor B2 phases. Note that three phase transformation events detected by the DSC heating curves are consistent with the three phases confirmed by XRD. However, four exothermic events were found in the cooling process. The first two peaks ranged from 1305 to 1153 °C correspond to the phase formation of the B2 and BCC phases, indicating that the liquidus temperature of the alloy occurs above 1305 °C. The latter two peaks arose from 1068 to 976 °C both originated from the phase formation of the Cu-rich phase.

On base of the DSC curves, the phase evolution in the CoFeTiVCu HEA during solidification can be sketched in Fig. 5b–e.

The alloy displays a liquid state above 1305 °C (Fig. 5b). As is well known, the elemental distribution and structural evolution of an HEA notably depend on both the entropy and enthalpy, and the alloy tend to decompose into multiple solid solution and/or intermetallic phases if there are large positive or negative mixing enthalpies between constituent elements [19]. The low negative mixing enthalpies of Co/Fe with Ti and large positive mixing enthalpies of Cu with the constituted elements accelerate the segregation of Cu in the alloy melt above the liquidus temperature [22]. The elemental preferred short-range ordering exists spontaneously in the liquid, e.g., noticeably Cu–Cu nearest-neighbor pairs confirmed by both the neutron diffraction experiment and ab initio molecular dynamics simulation, which can be viewed as the precursor for nucleating the segregated Cu-rich phase and is preserved in the FCC solid solution phase of the Cu-containing HEA [19]. Thus, during the early stage of solidification (1153–1305 °C, Fig. 5c), the B2 and primary BCC phases solidified from the liquid and were maintained in equilibrium with the Cu-rich liquid; in the temperature range of 1006–1068 °C (Fig. 5d), the large micron scale Cu-rich phases (lath and irregular shapes) nucleated and grew directly from the Cu-rich liquid; when the temperature further decreased to 976–1006 °C (Fig. 5e), two-hierarchical FCC Cu-rich nanoparticles precipitated in the BCC supersaturated matrix via a mechanism of precipitation decomposition. This mechanism is different from the spinodal decomposition, which usually occurs without the structure change from the matrix to the decomposed phases, such as the FCC Cu-rich plate-like phase formed in the FCC matrix of the CoCrCu $_{0.5}$ NiAl $_{0.5}$ and CoCrCuNiAl $_{0.5}$ HEAs designed by Wang et al. [32, 55]. The occurrence of nanoscale Cu-rich precipitates in this work might be attributed to two reasons. First, it follows the decreased solubility of Cu in the BCC matrix due to the diminishing effect of high mixing entropy as the temperature decreases, which has been confirmed by multi-phase materials [19, 57]. The low forming temperature of Cu-rich nanoprecipitates coincides with the 976–1006 °C temperature range of the fourth exothermic event. On the other hand, the diffusion rate of Cu is relatively fast according to simulated

Fig. 5 DSC curves **a** and the sketch diagram of phase evolving in the CoFeTiVCu alloy during solidification **b–e**



results [19, 58], which may facilitate further precipitation through Cu diffusion from the matrix.

Traditionally, the strength of polycrystalline materials can be induced by the well-known strengthening mechanisms: solid solution strengthening, grain refinement strengthening, dislocation strengthening, and precipitation strengthening [8]. The theoretical yield strength can be expressed by the following equation [59]:

$$\sigma_y = \sigma_0 + \Delta\sigma_{gb} + \Delta\sigma_{dis} + \Delta\sigma_{ss} + \Delta\sigma_{ps} \tag{1}$$

where σ_y is the theoretical yield strength, σ_0 is the lattice-friction stress, and $\Delta\sigma_{gb}$, $\Delta\sigma_{dis}$, $\Delta\sigma_{ss}$, and $\Delta\sigma_{ps}$ are strengthening increments from grain boundary, dislocation, solid solution, and precipitates. σ_0 can be calculated by rule-of-mixtures $\sigma_0 = f_{BCC} \sum c_i \sigma_{0.2i} + f_{FCC} \sum c_i \sigma_{0.2i}$, using the mole fraction c_i of i element in the BCC matrix or FCC Cu-rich precipitates and the yield strength $\sigma_{0.2i}$ of pure metal i (Table 3) [60], which was calculated as ~ 170 MPa for the present alloy. For grain boundary strengthening, the strength increments, $\Delta\sigma_{gb}$, can be well described by the classical Hall–Petch relationship as:

$$\Delta\sigma_{gb} = K^{HP} d^{-1/2} \tag{2}$$

where K^{HP} is the Hall–Petch coefficient with an estimated value of $250 \text{ MPa}\cdot\mu\text{m}^{1/2}$ for BCC structured HEAs [61, 62] and d is the average grain size. According to EBSD IPF map, the CoFeTiVCu sample exhibits a typical columnar crystal feature, and the average length and width of the grains are calculated to be $\sim 400 \mu\text{m}$ and $20 \mu\text{m}$ by quantitative metallography method. For simplicity, the mean grain size was approximated by the sqrt of the product of the average length and width with the value of $\sim 90 \mu\text{m}$. Then, the yield strength associated with $\Delta\sigma_{gb}$ was calculated as ~ 26 MPa. For dislocation strengthening, strength increments depend on dislocation density, which is proportional to micro strain. Its value can be obtained from the XRD pattern of the sample through the Williamson–Hall method, approaching to 0 in the as-cast HEAs [8, 55]. Hence, it is reasonable to regard the dislocation density as zero and the strengthening contribution from dislocation is evaluated as $\Delta\sigma_{dis} = 0$ for the as-cast CoFeTiVCu HEA.

For solid solution strengthening, the related strength is mainly associated with the atomic size misfit parameter, δ_a , and the modulus misfit parameter, δ_G , of the solute

Table 3 The atomic radius (r), shear modulus (G), and yield strength ($\sigma_{0.2}$) of pure metal in CoFeTiVCu HEA [60]

Element/property	Co	Fe	Ti	V	Cu
r (pm)	125.1	124.12	146.15	136.1	127.8
G (GPa)	69.8	65.3	41.7	60.8	53
$\sigma_{0.2}$ (MPa)	345	120	140	170	54

and solvent atoms in dilute solid solutions. According to the 9-atom cluster model and pseudo-binary solid solution approach proposed by Senkov et al., we can roughly estimate the δ_{ai} and δ_{Gi} of i element in a concentrated BCC phase in HEAs based on the average value of the atomic size difference and shear modulus difference, δ_{aij} and δ_{Gij} , between i and its eight nearest-neighbor atoms j [63, 64]. Based on the atomic radii, r_i , and shear moduli, G_i , of pure metals [60], as seen in Table 3, δ_{aij} , δ_{Gij} , δ_{ai} , and δ_{Gi} can be calculated and given in Tables 4 and 5. The calculated δ_{aij} shows that the pairs of Ti and Co, Fe, Cu have high atomic size differences ($|\delta_{aij}| \sim 0.13\text{--}0.16$) and δ_{Gij} displays a similar trend of Ti and Co, Fe, V ($|\delta_{Gij}| \sim 0.37\text{--}0.50$). The maximum lattice-distortion near Ti atoms is estimated to be $\delta_{aTi} \approx 0.181$, which originates from the difference between the local compression strains ($\delta_{aij} \sim 0.114$) of larger atom Ti and the local tension strains ($\delta_{aij} \sim -0.07$) of smaller atoms Co and Fe. Similarly, maximum modulus distortion was also caused by Ti, which is $|\delta_{GTi}| \approx 0.355$. Thus, a pseudo-binary solid solution approach with Co, Fe, V, and Cu representing solvents and Ti as solute was used to estimate the strength increment ($\Delta\sigma_{ss-a} + \Delta\sigma_{ss-G}$) from atomic size and shear modulus distortions of Ti in this HEA. Depending on $\Delta\sigma_{ss-a} = 0.1G(\delta_{aTi})^{4/3} c_{Ti}^{2/3}$ and $\Delta\sigma_{ss-G} = 0.1G(\delta_{GTi})^{4/3} c_{Ti}^{2/3}$, their contributions were $\Delta\sigma_{ss-a} = 252$ MPa and $\Delta\sigma_{ss-G} = 618$ MPa, respectively, displaying the same order as that in HfNbTaTiZr BCC solid solution [63].

For precipitation strengthening, the Orowan mechanism accurately models when the particles are large or incoherent

Table 4 Atomic size difference, $\delta_{aij} = 2(r_i - r_j)/(r_i + r_j)$, and modulus difference, $\delta_{Gij} = 2(G_i - G_j)/(G_i + G_j)$ (bold numbers), of the alloying element pairs

Element ij , $\delta_{aij}/\delta_{Gij}$	Co	Fe	Ti	V	Cu
Co	0	0.07	0.50	0.14	0.27
Fe	-0.01	0	0.44	0.07	0.21
Ti	0.16	0.16	0	- 0.37	- 0.24
V	0.08	0.09	-0.07	0	0.14
Cu	0.02	0.03	-0.13	-0.06	0

Table 5 Calculated lattice-distortion, $\delta_{ai} = \frac{2}{8} \sum c_j \delta_{aij}$, and modulus-distortion, $\delta_{Gi} = \frac{2}{8} \sum c_j \delta_{Gij}$, near each element in the BCC lattice of the matrix in the CoFeTiVCu HEA

	Co	Fe	Ti	V	Cu
δ_{ai}	-0.061	-0.070	0.114	0.034	-0.037
δ_{Gi}	0.215	0.050	-0.355	0.062	-0.091

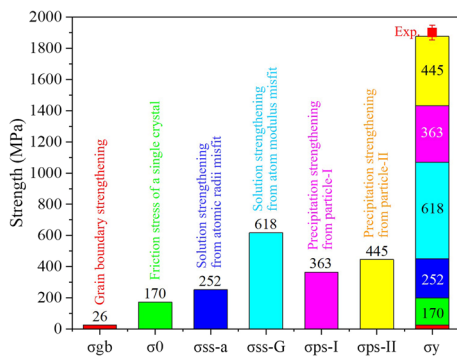


Fig. 6 Contributions of different strengthening mechanisms to yield strength of the CoFeTiVCu alloy

with the matrix while the shearing mechanism occurs when the precipitates are coherent and small [8]. Based on the size of Cu-rich precipitates in the matrix, the Orowan mechanism dominates in the CoFeTiVCu alloy and $\Delta\sigma_p$ can be calculated as [65]:

$$\Delta\sigma_p = \Delta\sigma_{Orowan} = M \times \frac{0.4Gb}{\pi\sqrt{1-\nu}} \times \frac{\ln\left(2\sqrt{2/3}r/b\right)}{\lambda_p} \quad (3)$$

where M is the Taylor Factor, ν is the Poisson's ratio, G is the shear modulus, and b is the Burger's vector of the BCC matrix ($M=2.73$, $\nu=0.3$ [65]; $G=66.5$ GPa, $b=0.256$ nm from experiments). $\lambda_p=2\sqrt{2/3}r\times(\sqrt{\pi/4f}-1)$ is the inter-precipitate spacing of Cu-rich phase and calculated by the average size r of precipitates obtained by ImageJ software. The volume fraction f of precipitates was detected by the EBSD phase map. Accordingly, the yield strength contributed by σ_0 , $\Delta\sigma_{gb}$, $\Delta\sigma_{ss-a}$, $\Delta\sigma_{ss-G}$, $\Delta\sigma_{p-I}$, $\Delta\sigma_{p-II}$ in the CoFeTiVCu alloy was calculated as ~ 170 , 26 , 252 , 618 , 363 , and 445 MPa, respectively, as seen in Fig. 6. The theoretical yield strength was 1874 MPa in total, which agreed well with the experimental (exp.) strength 1900 ± 30 MPa, indicating that the strengthening mainly stemmed from solution strengthening and precipitate strengthening.

4 Conclusion

In summary, hierarchical Cu-rich precipitates were found in a Cu-containing CoFeTiVCu HEA, and its evolution during solidification was intensively profiled. Meanwhile, the mechanical properties of the alloy with hierarchical Cu-rich precipitates were carefully investigated. The main conclusions are obtained as follows:

- (1) The CoFeTiVCu HEA was mainly composed of the Cu-rich FCC precipitates with three typical morphologies,

including nanoparticles, lath, and irregular shapes, and the BCC matrix.

- (2) The microstructural morphology displayed typical columnar crystals solidified from the cylindrical surface towards the center, which grew along the preferred orientation of the $\langle 101 \rangle$ and $\langle 001 \rangle$ of BCC crystals.
- (3) The precipitation of nanoscale Cu-rich particles was attributed to the decreased solubility of Cu in the BCC supersaturated matrix as the temperature decreased and the fast diffusion constant of Cu in the CoFeTiVCu HEA.
- (4) The precipitation strengthening of hierarchical precipitates together with the solid solution strengthening is responsible for the enhanced yield strength in the CoFeTiVCu HEA, resulting in higher strengths than most CoFeCu-based HEAs.

Acknowledgements Financial supports from Changzhou Science and Technology Bureau (No. CJ20220057, CJ20210065, CQ20210086), Postgraduate Research & Practice Innovation Program of Jiangsu Province (SJCX22_1464), and Postgraduate Practice and Innovation Projects of Jiangsu University of Technology (XSJCX22_03) are gratefully acknowledged.

Declarations

Conflict of interest The authors declare that they have no known competing financial interests or personal relationships that could have appeared to influence the work reported in this paper.

References

1. D.B. Miracle, O.N. Senkov, *Acta Mater.* **122**, 448–511 (2017)
2. J.W. Yeh, S.K. Chen, S.J. Lin, J.Y. Gan, T.S. Chin, T.T. Shun, C.H. Tsau, S.Y. Chang, *Adv. Eng. Mater.* **6**, 299–303 (2004)
3. B. Cantor, I.T.H. Chang, P. Knight, A.J.B. Vincent, *Mater. Sci. Eng. A* **375–377**, 213–218 (2004)
4. Y.J. Zhou, Y. Zhang, Y.L. Wang, G.L. Chen, *Appl. Phys. Lett.* **90**, 181904 (2007)
5. C.-C. Juan, M.-H. Tsai, C.-W. Tsai, C.-M. Lin, W.-R. Wang, C.-C. Yang, S.-K. Chen, S.-J. Lin, J.-W. Yeh, *Intermetallics* **62**, 76–83 (2015)
6. F. Otto, A. Dlouhý, C. Somsen, H. Bei, G. Eggeler, E.P. George, *Acta Mater.* **61**, 5743–5755 (2013)
7. S. Niu, H. Kou, T. Guo, Y. Zhang, J. Wang, J. Li, *Mater. Sci. Eng. A* **671**, 82–86 (2016)
8. J.Y. He, H. Wang, H.L. Huang, X.D. Xu, M.W. Chen, Y. Wu, X.J. Liu, T.G. Nieh, K. An, Z.P. Lu, *Acta Mater.* **102**, 187–196 (2016)
9. Y.J. Liang, L. Wang, Y. Wen, B. Cheng, Q. Wu, T. Cao, Q. Xiao, Y. Xue, G. Sha, Y. Wang, Y. Ren, X. Li, L. Wang, F. Wang, H. Cai, *Nat. Commun.* **9**, 4063 (2018)
10. M. Wang, Y. Lu, T. Wang, C. Zhang, Z. Cao, T. Li, P.K. Liaw, *Scr. Mater.* **204**, 114132 (2021)
11. Y. Lu, X. Gao, L. Jiang, Z. Chen, T. Wang, J. Jie, H. Kang, Y. Zhang, S. Guo, H. Ruan, Y. Zhao, Z. Cao, T. Li, *Acta Mater.* **124**, 143–150 (2017)

12. T. Yang, Y.L. Zhao, Y. Tong, Z.B. Jiao, J. Wei, J.X. Cai, X.D. Han, D. Chen, A. Hu, J.J. Kai, K. Lu, Y. Liu, C.T. Liu, *Science* **362**, 933–937 (2018)
13. X. Xian, L. Lin, Z. Zhong, C. Zhang, C. Chen, K. Song, J. Cheng, Y. Wu, *Mater. Sci. Eng. A* **713**, 134–140 (2018)
14. D.E. Jodi, N. Park, *Mater. Lett.* **255**, 126528 (2019)
15. G. Qin, R. Chen, P.K. Liaw, Y. Gao, X. Li, H. Zheng, L. Wang, Y. Su, J. Guo, H. Fu, *Scr. Mater.* **172**, 51–55 (2019)
16. B. Ren, Z.X. Liu, D.M. Li, L. Shi, B. Cai, M.X. Wang, *J. Alloy. Compd.* **493**, 148–153 (2010)
17. B. Wu, Z. Xie, J. Huang, J. Lin, Y. Yang, L. Jiang, J. Huang, G. Ye, C. Zhao, S. Yang, B. Sa, *Intermetallics* **93**, 40–46 (2018)
18. S. Singh, N. Wanderka, B.S. Murty, U. Glatzel, J. Banhart, *Acta Mater.* **59**, 182–190 (2011)
19. L.J. Santodonato, Y. Zhang, M. Feygenson, C.M. Parish, M.C. Gao, R.J. Weber, J.C. Neufeind, Z. Tang, P.K. Liaw, *Nat. Commun.* **6**, 5964 (2015)
20. P. Agrawal, S. Gupta, S. Shukla, S.S. Nene, S. Thapliyal, M.P. Toll, R.S. Mishra, *Mater. Des.* **215**, 110487 (2022)
21. S.M. Oh, S.I. Hong, *Mater. Chem. Phys.* **210**, 120–125 (2018)
22. A. Takeuchi, A. Inoue, *Mater. Trans.* **46**, 2817–2829 (2005)
23. Z. Wu, M. Chen, B. Li, M. Lv, R. Zheng, Y. Yang, X. Tan, H. Xu, *Mater. Character.* **191**, 112161 (2022)
24. D. Choudhuri, T. Alam, T. Borkar, B. Gwalani, A.S. Mantri, S.G. Srinivasan, M.A. Gibson, R. Banerjee, *Scr. Mater.* **100**, 36–39 (2015)
25. R. Song, F. Ye, C. Yang, S. Wu, *J. Mater. Sci. Technol.* **34**, 2014–2021 (2018)
26. X.F. Wang, Y. Zhang, Y. Qiao, G.L. Chen, *Intermetallics* **15**, 357–362 (2007)
27. F.J. Wang, Y. Zhang, G.L. Chen, *J. Alloy. Compd.* **478**, 321–324 (2009)
28. R. Sonkusare, R. Jain, K. Biswas, V. Parameswaran, N.P. Gurao, *J. Alloy. Compd.* **823**, 153763 (2020)
29. Y. Zhuang, W. Liu, P. Xing, F. Wang, J. He, *Acta Metall. Sin.* **25**, 124–130 (2012)
30. B.S. Li, Y.P. Wang, M.X. Ren, C. Yang, H.Z. Fu, *Mater. Sci. Eng. A* **498**, 482–486 (2008)
31. Y. Yu, N. Xu, S. Zhu, Z. Qiao, J. Zhang, J. Yang, W. Liu, *J. Mater. Sci. Technol.* **69**, 48–59 (2021)
32. M. Wang, G. Zhang, H. Cui, Y. Lu, Y. Zhao, N. Wei, T. Li, *J. Mater. Sci.* **56**, 5878–5898 (2021)
33. J.W. Choi, J.T. Kim, S.H. Hong, H.J. Park, E. Jumaev, K.B. Kim, *J. Alloy. Compd.* **928**, 166999 (2022)
34. J.M. Zhu, H.F. Zhang, H.M. Fu, A.M. Wang, H. Li, Z.Q. Hu, *J. Alloy. Compd.* **497**, 52–56 (2010)
35. F.J. Wang, Y. Zhang, G.L. Chen, H.A. Davies, *J. Eng. Mater. Technol.* **131**, 034501 (2009)
36. M. Wang, Z. Wen, B. Ma, J. Liu, Z. Zou, Y. Zhao, *J. Alloy. Compd.* **893**, 162242 (2022)
37. Y. Zhang, M. Liu, J. Sun, G. Li, R. Zheng, W. Xiao, C. Ma, *Mater. Sci. Eng. A* **835**, 142670 (2022)
38. S.S. Sohn, A. Kwiatkowski da Silva, Y. Ikeda, F. Kormann, W. Lu, W.S. Choi, B. Gault, D. Ponge, J. Neugebauer, D. Raabe, *Adv. Mater.* **31**, 1807142 (2019)
39. G. Laplanche, A. Kostka, O.M. Horst, G. Eggeler, E.P. George, *Acta Mater.* **118**, 152–163 (2016)
40. Z. An, S. Mao, Y. Liu, L. Wang, H. Zhou, B. Gan, Z. Zhang, X. Han, *J. Mater. Sci. Technol.* **79**, 109–117 (2021)
41. J.P. Couzinié, L. Lilensten, Y. Champion, G. Dirras, L. Perrière, I. Guillot, *Mater. Sci. Eng. A* **645**, 255–263 (2015)
42. L. Lilensten, J.P. Couzinié, L. Perrière, A. Hocini, C. Keller, G. Dirras, I. Guillot, *Acta Mater.* **142**, 131–141 (2018)
43. H. Jiang, D. Qiao, W. Jiao, K. Han, L. Yiping, P.K. Liaw, *J. Mater. Sci. Technol.* **61**, 119–124 (2021)
44. X. Gao, Y. Lu, B. Zhang, N. Liang, G. Wu, G. Sha, J. Liu, Y. Zhao, *Acta Mater.* **141**, 59–66 (2017)
45. W. Jiao, T. Li, X. Chang, Y. Lu, G. Yin, Z. Cao, T. Li, *J. Alloy. Compd.* **902**, 163814 (2022)
46. Y. Zhao, X. Fu, Y. Lu, Q. Yu, *Mater. Today NANO* **20**, 100263 (2022)
47. H. Yang, Y. Bu, J. Wu, Y. Fang, J. Liu, H. Wang, W. Yang, *Mater. Character.* **176**, 111099 (2021)
48. C. Zhou, C. Guo, C. Li, Z. Du, *Calphad* **63**, 61–76 (2018)
49. L. Mineau, S. Hamar-Thibault, C.H. Allibert, *Phys. Status Solidi A* **134**, 93–105 (1992)
50. N. Derimow, R.F. Jaime, B. Le, R. Abbaschian, *Mater. Chem. Phys.* **261**, 124190 (2021)
51. J.A. Wollmershauser, C.J. Neil, S.R. Agnew, *Metal. Mater. Trans. A* **41**, 1217–1229 (2009)
52. L. Ma, T. Cao, J. Wang, Y. Xue, H. Yu, *Mater. Res. Express* **6**, 1065h1064 (2019)
53. J. Yi, L. Wang, L. Zeng, M. Xu, L. Yang, S. Tang, *Int. J. Refract. Met. H.* **95**, 105416 (2021)
54. X.H. Lin, W.L. Johnson, *J. Appl. Phys.* **78**, 6514–6519 (1995)
55. M. Wang, H. Cui, Y. Zhao, C. Wang, N. Wei, Y. Zhao, X. Zhang, Q. Song, *Mater. Des.* **180**, 107893 (2019)
56. W.L. Wang, Z.H. Kong, *J. Alloy. Compd.* **853**, 156451 (2021)
57. C.-J. Tong, Y.-L. Chen, S.-K. Chen, J.-W. Yeh, T.-T. Shun, C.-H. Tsau, S.-J. Lin, S.-Y. Chang, *Metal. Mater. Trans. A* **36**, 881–893 (2005)
58. A. Seoane, D. Farkas, X.-M. Bai, *J. Mater. Res.* **37**, 1403–1415 (2022)
59. M.Y. Chen, M. Gouné, M. Verdier, Y. Bréchet, J.R. Yang, *Acta Mater.* **64**, 78–92 (2014)
60. Goodfellow Index of Materials: <http://www.goodfellow.com/E/T.html>.
61. S. Chen, K.-K. Tseng, Y. Tong, W. Li, C.-W. Tsai, J.-W. Yeh, P.K. Liaw, *J. Alloy. Compd.* **795**, 19–26 (2019)
62. C.-C. Juan, M.-H. Tsai, C.-W. Tsai, W.-L. Hsu, C.-M. Lin, S.-K. Chen, S.-J. Lin, J.-W. Yeh, *Mater. Lett.* **184**, 200–203 (2016)
63. O.N. Senkov, J.M. Scott, S.V. Senkova, D.B. Miracle, C.F. Woodward, *J. Alloy. Compd.* **509**, 6043–6048 (2011)
64. O.N. Senkov, A.L. Pilchak, S.L. Semiatin, *Metal. Mater. Trans. A* **49**, 2876–2892 (2018)
65. C. Li, Y. Ma, J. Hao, Y. Yan, Q. Wang, C. Dong, P.K. Liaw, *Mater. Sci. Eng. A* **737**, 286–296 (2018)

Publisher's Note Springer Nature remains neutral with regard to jurisdictional claims in published maps and institutional affiliations.

Springer Nature or its licensor (e.g. a society or other partner) holds exclusive rights to this article under a publishing agreement with the author(s) or other rightsholder(s); author self-archiving of the accepted manuscript version of this article is solely governed by the terms of such publishing agreement and applicable law.